Electronic structure, magnetic correlations, and superconducting pairing in the reduced Ruddlesden-Popper bilayer La$_3$Ni$_2$O$_6$ under pressure: Different role of $d_{3z^2-r^2}$ orbital compared with La$_3$Ni$_2$O$_7$

Yang Zhang [1], Ling-Fang Lin [1], Adriana Moreo [1,2], Thomas A. Maier [3], and Elbio Dagotto [1,2]

[1]*Department of Physics and Astronomy, University of Tennessee, Knoxville, Tennessee 37996, USA*

[2]*Materials Science and Technology Division, Oak Ridge National Laboratory, Oak Ridge, Tennessee 37831, USA*

[3]*Computational Sciences and Engineering Division, Oak Ridge National Laboratory, Oak Ridge, Tennessee 37831, USA*

The recent discovery of superconductivity in bilayer La$_3$Ni$_2$O$_7$ (327-LNO) under pressure stimulated much interest in layered nickelates. However, superconductivity was not found in another bilayer nickelate system, La$_3$Ni$_2$O$_6$ (326-LNO), even under pressure. To understand the similarities and differences between 326-LNO and 327-LNO, using density functional theory and the random phase approximation (RPA), we systematically investigate 326-LNO under pressure. The large crystal-field splitting between the e_g orbitals caused by the missing apical oxygen moves the $d_{3z^2-r^2}$ orbital farther away from the Fermi level, implying that the $d_{3z^2-r^2}$ orbital plays a less important role in 326-LNO than in 327-LNO. This also results in a smaller bandwidth for the $d_{x^2-y^2}$ orbital and a reduced energy gap for the bonding-antibonding splitting of the $d_{3z^2-r^2}$ orbital in 326-LNO, as compared to 327-LNO. Moreover, the in-plane hybridization between the $d_{x^2-y^2}$ and $d_{3z^2-r^2}$ orbitals is found to be small in 326-LNO, while it is much stronger in 327-LNO. Furthermore, the low-spin ferromagnetic state is found to be the likely ground state in 326-LNO under high pressure. The weak interlayer coupling suggests that $s_\pm$-wave pairing is unlikely in 326-LNO. The robust in-plane ferromagnetic coupling also suggests that d-wave superconductivity, which is usually caused by antiferromagnetic fluctuations of the $d_{x^2-y^2}$ orbital, is also unlikely in 326-LNO. These conclusions are supported by our many-body RPA calculations of the pairing behavior. In addition, for the bilayer cuprate HgBa$_2$CaCu$_2$O$_6$, we find a strong self-doping effect of the $d_{x^2-y^2}$ orbital under pressure, with the charge of Cu being reduced by approximately 0.13 electrons from 0 GPa to 25 GPa. In contrast, we do not observe such a change in the electronic density in 326-LNO under pressure, establishing another important difference between the nickelates and the cuprates.

I. INTRODUCTION

The recent experimental discovery of pressure-induced superconductivity in the Ruddlesden-Popper bilayer (RP-BL) perovskite La$_3$Ni$_2$O$_7$ (327-LNO) [1] opened a platform for understanding and studying layered nickel-based high-temperature superconductors [2–42]. The compound 327-LNO has an orthorhombic structure with a stacked bilayer NiO$_6$ octahedron sublattice geometry, where superconductivity with the highest T_c up to 80 K was reported in the high-pressure phase [see Fig. 1(a)] [1].

Under the influence of hydrostatic pressure, the structure of 327-LNO transforms from *Amam* to *Fmmm* symmetry followed by the stabilization of a superconducting phase for a broad range of pressures from 14 to 43.5 GPa [1]. The electronic density of Ni is $n = 7.5$ in 327-LNO, corresponding to Ni$^{2.5+}$ on average, resulting in two e_g orbitals ($d_{x^2-y^2}$ and $d_{3z^2-r^2}$) contributing to the Fermi surface (FS) based on density functional theory (DFT) calculations [2,3]. The $d_{x^2-y^2}$ orbital is nearly quarter filled and the $d_{3z^2-r^2}$ orbital is closed to half filled, establishing a two-orbital minimum model. In addition, the partial nesting of the FSs for wave vectors $(\pi,0)$ and $(0,\pi)$ favors $s_\pm$-wave superconductivity induced by the strong interlayer coupling in 327-LNO, as discussed in recent

theoretical efforts [4–6,8,9,13,14,29,31,35,37]. Other studies alternatively suggested the possibility of d-wave pairing superconductivity [24,30,36], as in the cuprates.

By chemical reduction, namely, removal of the apical oxygen from 327-LNO, the compound La$_3$Ni$_2$O$_6$ (326-LNO) was obtained experimentally. 326-LNO also has a stacking Ni bilayer structure [see Fig. 1(b)] but displays the NiO$_2$ square-planar bilayer sublattice. The material 326-LNO reminds us of the previously well-studied bilayer superconducting cuprates HgBa$_2$CaCu$_2$O$_6$ (12126-HBCCO) [43], with a similar CuO$_2$ square-planar bilayer sublattice [see Fig. 1(c)]. The difference between reduced RP-BL and RP-BL structures is that there are no additional apical O atoms connecting two Ni or Cu layers in the reduced RP-BL lattice, as shown in Figs. 1(d) and 1(e).

At ambient pressure, no long-range magnetic order was found down to 4 K for 326-LNO [44] but the existence of magnetic correlations was observed in the powder samples by nuclear magnetic resonance [45]. Furthermore, weak ferromagnetic (FM) tendencies were also reported in 326-LNO at 5 K that persist at least up to 400 K [44]. This is considered to be related to nearly degenerate FM and antiferromagnetic (AFM) states [44,46]. In addition, a checkerboard charge-ordered insulating state with AFM coupling was also predicted in 326-LNO [47]. However, due to the intrinsic
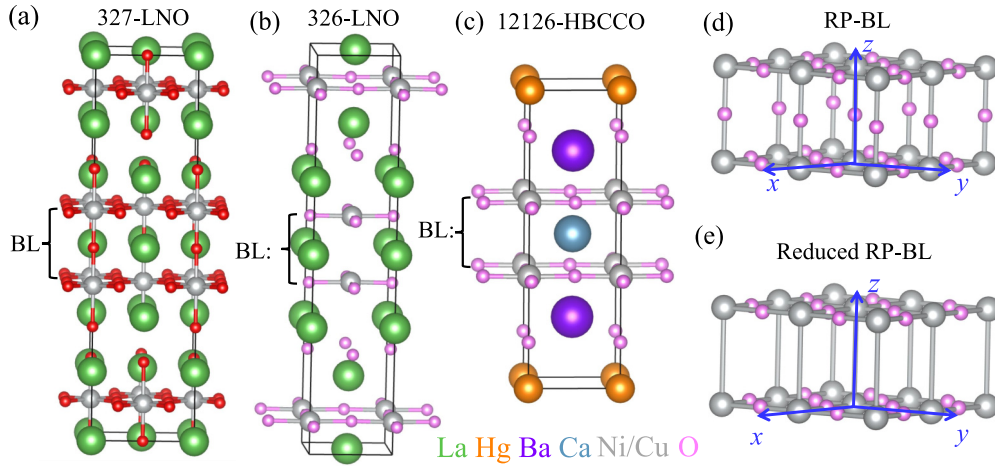
FIG. 1. (a)–(c) Schematic crystal structures of the conventional cell of (a) 327-LNO, (b) 326-LNO, and (c) 12126-HBCCO (green: La; orange: Hg; violet: Ba; sky blue: Ca; gray: Ni or Cu; pink: O). (d), (e) Sketch of the bilayer structures studied here: (d) RP-BL sublattice with NiO$_6$ plane; (e) Reduced RP-BL sublattice with NiO$_4$ or CuO$_4$ planes. The local z axis is perpendicular to the planes, while the local x or y axis is along the in-plane Ni–O or Cu–O bond directions, resulting in $d_{x^2-y^2}$ orbitals lying in the layer plane.

limitations of powder samples [44], the AFM charge-order instability was not confirmed yet. Of primary importance for the work discussed here, contrary to the pressure-induced superconductivity of 327-LNO, superconductivity was not observed in 326-LNO under pressure up to a maximum of 25.3 GPa, although an insulator-metal transition was found around 6.1 GPa in recent experiments [48].

Considering these studies in bilayer systems, several interesting questions naturally arise: What are the similarities and differences between the bilayer 326-LNO and 327-LNO nickelates under pressure? What causes these differences? Does the missing apical oxygen in 326-LNO play a key role in the reported absence of superconductivity under pressure? What is the connection between 326-LNO and 12126-HBCCO?

To address these questions, here we theoretically study the 326-LNO compound under pressure by using first-principles DFT as well as random phase approximation (RPA) calculations. Similarly to 327-LNO, pressure increases the bandwidth of the Ni's $3d$ states, leading to an enhanced itinerant behavior and thus effectively reduced electronic correlations. Furthermore, the Ni's $3d$ orbitals are mainly located near the Fermi level and most of the O's $2p$ states are far away from that Fermi level, indicating a robust charge-transfer energy ($\varepsilon_d - \varepsilon_O$) in both 326-LNO and 327-LNO, establishing a common character among these nickelates. In addition, the $d_{3z^2-r^2}$ orbital displays a bonding-antibonding splitting character in both 326-LNO and 327-LNO, as well as in 12126-HBCCO.

However, different from 327-LNO, the crystal-field splitting between the e_g orbitals is much larger in 326-LNO and also the in-plane hybridization between the $d_{x^2-y^2}$ and $d_{3z^2-r^2}$ orbitals was found to be very small in the latter, leading to only two FS sheets, α and β, composed primarily of the single $d_{x^2-y^2}$ orbital. By introducing electronic correlations, the low-spin FM state was found to have the lowest energy among the five considered candidates under pressure, with a very weak magnetic coupling between the layers. This strongly suggests

that $s_\pm$-wave pairing is unlikely in 326-LNO. Furthermore, the large in-plane FM coupling also indicates that d-wave superconductivity, usually caused by AFM fluctuations of the $d_{x^2-y^2}$ orbital, is also unlikely in 326-LNO. These qualitative conclusions are supported by our many-body RPA calculations that 326-LNO system should not have a superconducting state. In addition, we do not observe any obvious changes of the electronic density in 326-LNO under pressure, while there is a strong self-doping effect of the $d_{x^2-y^2}$ orbital in 12126-HBCCO, establishing another difference between the nickelates and the cuprates.

II. METHOD

In the present paper, the first-principles DFT calculations were performed by using the VIENNA AB INITIO SIMULATION PACKAGE code, within the projector augmented wave (PAW) method [49–51], with the generalized gradient approximation and the Perdew-Burke-Ernzerhof (PBE) exchange potential [52]. The plane-wave cutoff energy was set as 550 eV.

Both lattice constants and atomic positions were fully relaxed until the Hellman-Feynman force on each atom was smaller than 0.01 eV/Å. The k-point mesh was appropriately modified for different crystal structures to make the k-point densities approximately the same in reciprocal space (e.g., $16 \times 16 \times 3$ for the conventional structure of 326-LNO in the $I4/mmm$ phase). In addition to the standard DFT calculation, we employed the maximally localized Wannier functions (MLWFs) method to fit the Ni's e_g bands to obtain the hoppings and crystal-field splittings for our subsequent model RPA calculations, as well as obtaining the FSs, using the WANNIER90 packages [53]. Furthermore, the calculated three-dimensional FSs obtained from MLWFs were visualization by XCRYSDEN package [54]. All crystal structures were visualized with the VESTA code [55].

To discuss the magnetic tendencies in 327-LNO under pressure, a strong intra-atomic interaction was considered in

a screened Hartree-Fock-like manner, as used in the local density approach (LDA) plus U method with Liechtenstein format within the double-counting item [56]. In addition, specific values for $U = 4.75$ eV and $J = 0.68$ eV were considered in our study of 326-LNO, as used in a previous study [47,57].

To investigate the superconducting pairing properties of the 326-LNO system, we first constructed a four-band e_g orbital tight-binding model on a bilayer lattice [58–61], involving two Ni sites with e_g orbitals in a unit cell with an overall filling of $n = 5$. The kinetic hopping component of the Hamiltonian is

$$H_k = \sum_{\substack{i\sigma \\ \bar{\alpha}\gamma\gamma'}} t_{\gamma\gamma'}^{\bar{\alpha}}(c_{i\sigma\gamma}^{\dagger}c_{i+\bar{\alpha}\sigma\gamma'} + \text{H.c.}) + \sum_{i\gamma\sigma}\Delta_{\gamma}n_{i\gamma\sigma}. \quad (1)$$

The first term represents the hopping of an electron from orbital γ at site i to orbital γ' at the neighboring site $i + \bar{\alpha}$. $c_{i\sigma\gamma}^{\dagger}$ ($c_{i\sigma\gamma}$) is the standard creation (annihilation) operator, γ and γ' represent the different orbitals, and σ is the z-axis spin projection. Δ_{γ} represents the crystal-field splitting of each orbital γ. The vectors $\bar{\alpha}$ are along the three bilayer-lattice directions [see Fig. 1(e)], defining different neighbors of hoppings (the detailed hoppings can be found in the Supplemental Material [62]).

This Hamiltonian is supplemented with an interaction term that contains on-site intraorbital U and interorbital U' Coulomb repulsions as well as Hund's coupling J and pair-hopping J' terms. To assess this model for its pairing behavior, we performed many-body RPA calculations, which are based on a perturbative weak-coupling expansion in the Coulomb interaction [63–66]. In our multiorbital RPA technique [63–65], the RPA enhanced spin susceptibility is obtained from the Lindhart function $\chi_0(\mathbf{q})$:

$$\chi(\mathbf{q}) = \chi_0(\mathbf{q})[1 - \mathcal{U}\chi_0(\mathbf{q})]^{-1}. \quad (2)$$

Here, $\chi_0(\mathbf{q})$ is an orbital-dependent susceptibility tensor and $\mathcal{U}$ is a tensor that contains the interaction parameters [64]. The pairing strength λ_{α} for channel α and the corresponding gap structure $g_{\alpha}(\mathbf{k})$ are obtained from solving an eigenvalue problem of the form

$$\int_{\text{FS}} d\mathbf{k}' \, \Gamma(\mathbf{k} - \mathbf{k}')g_{\alpha}(\mathbf{k}') = \lambda_{\alpha}g_{\alpha}(\mathbf{k}), \quad (3)$$

where the momenta $\mathbf{k}$ and $\mathbf{k}'$ are on the FS, and $\Gamma(\mathbf{k} - \mathbf{k}')$ contains the irreducible particle-particle vertex. In the RPA approximation, the dominant term entering $\Gamma(\mathbf{k} - \mathbf{k}')$ is the RPA spin susceptibility $\chi(\mathbf{k} - \mathbf{k}')$.

Note that, in our RPA calculation, we solved a simplified version of the linearized Eliashberg equation, in which the Matsubara frequency dependence has already been summed over. Our RPA approach is based on the Bardeen-Cooper-Schrieffer assumption that the spin-fluctuation pairing interaction is approximately independent of energy in a shell around the FS up to an energy cutoff ω_0 and given by its static limit. Based on this assumption, the Matsubara sum in the Eliashberg equations can be performed analytically, and one arrives at an equation formally represented by Eq. (3) without frequency dependence in which only the states on the FS enter.

More details of this procedure have been well discussed in Ref. [67]. This approach is much less demanding than solving the full Eliashberg equations, and it has already been routinely used in previous literatures of unconventional superconductors, such as iron-based superconductors [64]. In our present paper, there are no other low-lying states or incipient bands that are not represented by the Fermi surface states as displayed in the electronic structure. Thus, we do not expect that a treatment including energy dependence, and such potential states, to give qualitatively different results. Here, we used a total of 160 k points on the FS, and we checked that the results converged with respect to the number of k points.

III. RESULTS

A. Electronic structures and Fermi surface

In the pressure range that we studied, the electronic structures of 326-LNO remain very similar in shape, while pressure increases the bandwidth of the Ni's $3d$ states, leading to an enhanced itinerant behavior. This larger bandwith effectively reduces the electronic correlations (see Appendix). Here, unless otherwise specified, we will mainly focus on the results at 25 GPa to understand the similarities and differences between the bilayer 326-LNO and 327-LNO systems. At this pressure, 327-LNO is already superconducting but 326-LNO is not [68].

As shown in Figs. 2(a) and 2(b), in both 326-LNO and 327-LNO, the Ni's $3d$ orbitals are those that primarily contribute to the electronic density near the Fermi level, hybridized with O p-states. Furthermore, the O p-states are mainly located in lower energy regions than the Ni's $3d$ states, indicating a large charge-transfer gap between Ni's $3d$ and O's $2p$ orbitals (ε_d - ε_O). This is similar to what we found in our previous study of the infinite-layer NdNiO$_2$ [69]. In addition, the three t_{2g} orbitals are fully occupied, while the $d_{x^2-y^2}$ is partially occupied crossing the Fermi level in both cases of 326-LNO and 327-LNO. Compared with 327-LNO, the $d_{x^2-y^2}$ orbital is less itinerant with a reduced bandwidth of $\sim20\%$ in the 326-LNO case, resulting in a reduced nearest-neighbor hopping for the $d_{x^2-y^2}$ orbital. This suggests that the additional apical oxygen connected to two Ni layers in 327-LNO enhances the itinerant behavior of the d orbitals, reducing the effective electronic correlations U/W in 327-LNO as compared to those of 326-LNO.

Furthermore, the Ni $d_{3z^2-r^2}$ orbital shows a bonding-antibonding molecular-orbital splitting character in both cases, caused by the dimer structure in the bilayers, as discussed in 327-LNO [3]. Compared with 327-LNO, the energy gap between bonding and antibonding states decreases by about 21% in 326-LNO, indicating that the bridge of the apical oxygen would increase the hopping and enhance the bonding-antibonding splitting. Hence, in both 326-LNO and 327-LNO, the $d_{3z^2-r^2}$ states are more localized and $d_{x^2-y^2}$ states are more itinerant.

Because there are no apical oxygens connecting two Ni sites between the two layers of bilayer 326-LNO, the crystal-field splitting Δ between the orbitals $d_{3z^2-r^2}$ and $d_{x^2-y^2}$ increases significantly (~1.96 eV) compared with that in 327-LNO (~0.51 eV) [9]. In this case, the interlayer magnetic coupling should be quite small in 326-LNO, suggesting a different role of the $d_{3z^2-r^2}$ orbital in those two systems, although they both have a bilayer Ni sublattice. Moreover, the in-plane interorbital hopping between the e_g orbitals is also
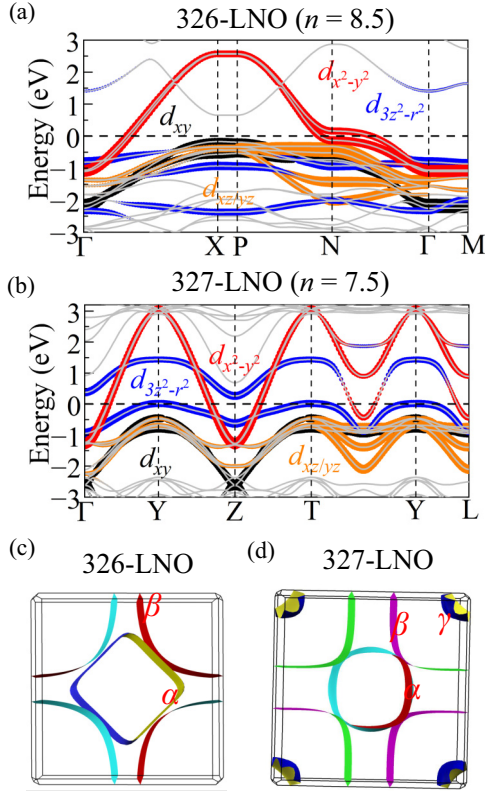
FIG. 2. Projected band structures of the nonmagnetic phase of (a) $I4/mmm$ 326-LNO and (b) $Fmmm$ 327-LNO structures without any electronic interaction, at 25 GPa. The weight of each Ni orbital is given by the size of the circles. The Fermi level (zero energy) is marked by the horizontal dashed line. The coordinates of the high-symmetry points of the Brillouin zone are (a) $\Gamma = (0, 0, 0)$, $X = (0, 0, 0.5)$, $P = (0.25, 0.25, 0.25)$, $N = (0, 0.5, 0)$, and $M = (0.5, 0.5, -0.5)$ for $I4/mmm$ 326-LNO and (b) $\Gamma = (0, 0, 0)$, $Y = (0.5, 0, 0.5)$, $Z = (0.5, 0.5, 0)$, $T = (0, 0.5, 0.5)$, and $L = (0.5, 0.5, 0.5)$ for $Fmmm$ 327-LNO. FSs of the (c) $I4/mmm$ 326-LNO and (d) $Fmmm$ 327-LNO at 25 GPa. The existence of γ pockets is clearly visible in 327-LNO but they are absent in 326-LNO.

rather small in 326-LNO ($\sim$0.013 eV), leading to a reduced in-plane hybridization between the $d_{3z^2-r^2}$ and $d_{x^2-y^2}$ orbitals compared to that in 327-LNO ($\sim$0.243 eV) [9].

As a result of these differences, in 326-LNO, only the $d_{x^2-y^2}$ orbital contributes to the FS, leading to two strongly two-dimensional sheets (α and β), as shown in Fig. 2(c). However, the FS of 327-LNO in the $Fmmm$ phase is made up of both $d_{x^2-y^2}$ and $d_{3z^2-r^2}$ orbitals, resulting in two sheets (α and β) and an additional pocket (γ). Due to the strong hybridization of the e_g states in 327-LNO, the two sheets α and β display a mixed character between the $d_{3z^2-r^2}$ and $d_{x^2-y^2}$ orbitals. Hence, $d_{3z^2-r^2}$ is not as important in the 326-LNO case as in 327-LNO, which may be crucial to understand the absence of superconductivity in the former.

B. Magnetic correlations in 326-LNO under pressure

Next, we introduce local Hubbard couplings and study the magnetic correlations in 326-LNO under pressure. For our studies, several magnetic structures of the Ni bilayer spins
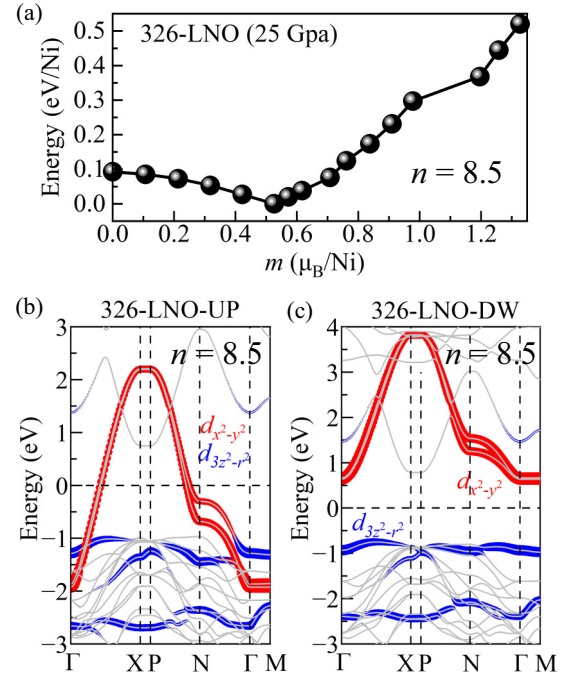
FIG. 3. (a) Total energy as a function of the magnetic moment of the Ni ions for 326-LNO at 25 GPa. (b), (c) Projected band structures of the FM phase in the $I4/mmm$ structural phase of 326-LNO for (b) spin up and (c) spin down at 25 GPa. The key e_g orbitals are marked by the red and blue colors. The Fermi level (zero energy) is marked by the horizontal dashed line.

were considered: (1) A-AFM: FM coupling in the NiO$_2$ layer plane and AFM coupling between the Ni layers; (2) FM: FM coupling along both the NiO$_2$ layer plane and between the Ni layers; (3) G-AFM: AFM coupling along both the NiO$_2$ layer plane and between the Ni layers; (4) C-AFM: AFM coupling along the NiO$_6$ layer plane and FM coupling between the layers; and (5) stripe-AFM: AFM in one in-plane direction and FM in the other, while the coupling along the Ni layers direction is AFM. For all these states, we used the specific values $U = 4.75$ eV and $J = 0.68$ eV for 326-LNO in the LDA + U format with a double-counting item [56] as used in a previous study of 326-LNO [47,57].

Considering the $d^{8.5}$ electronic configuration in 326-LNO and the square-planar crystal-field splitting, the Ni ions are expected to be in a low-spin state for 326-LNO. To confirm this, we calculated the total energy as a function of the magnetic moment of the Ni ions for 326-LNO at 25 GPa, using the fixed-spin-moment method. Figure 3(a) clearly shows an energy minimum around 0.53 μ_B/Ni, supporting the low-spin picture in 326-LNO.

Next, using the same crystal structure, we calculated the energies for different magnetic configurations. As shown in Table I, the FM state has the lowest energy among the five considered candidates. In addition, the energy difference between the A-AFM and FM states is quite small, indicating that the coupling between layers is weak in 326-LNO, while a strong AFM coupling was found in 327-LNO due to the large hopping amplitude of the $d_{3z^2-r^2}$ orbital between the layers [3,9]. The weak interlayer FM coupling in 326-LNO suggests that

TABLE I. Energy differences (meV/Ni) and calculated magnetic moment (μ_B/Ni) for the various input spin configurations used here. The FM configuration is taken as the energy of reference.

Magnetism	Energy	Magnetic moment
A-AFM	0.65	0.530
FM	0	0.526
G-AFM	107.92	0.208
C-AFM	104.00	0.212
stripe-AFM	43.91	0.455

$s_\pm$-wave pairing discussed in the context of 327-LNO may not be favored. Moreover, the C-AFM state has a much higher energy than the FM phase, indicating a large in-plane FM coupling in 326-LNO, while the in-plane magnetic coupling is much weaker in 327-LNO [3,9]. The in-plane strong FM coupling is expected to disfavor d-wave superconductivity, which is induced by in-plane AFM fluctuations of the $d_{x^2-y^2}$ orbitals. These considerations suggest that 326-LNO is far from a superconducting instability.

Due to the weak coupling between layers, this system is an effective single-layer system. Furthermore, the $d_{3z^2-r^2}$ orbital is fully occupied and has a large crystal-field splitting Δ with the $d_{x^2-y^2}$ orbital in the 326-LNO, indicating it is inactive. As a result, 326-LNO can be considered a single-orbital ($d_{x^2-y^2}$) two-dimensional model system with the electronic density $n = 0.5$. Here, our results found a strong in-plane FM coupling [70], also in agreement with the single-orbital two-dimensional Hubbard model results where the FM spin correlations were also found at $n = 0.5$ [71]. Different from 326-LNO, the $d_{3z^2-r^2}$ orbital is active in the 327-LNO material, leading to a strong AFM interlayer coupling. In addition, we found that the stripe-AFM state has a lower energy ($\sim$50 meV/Ni) than the FM state in 327-LNO [3]. This stripe state is caused by the competition between the intraorbital and interorbital hopping mechanisms [72,73], namely, to the competition of AFM and FM tendencies. Thus, the main different property between the 326-LNO and 327-LNO materials is having only one active orbital in the first versus two active orbitals in the second, namely, the $d_{3z^2-r^2}$ orbital displays quite different roles in these two systems. However, to better display the different roles of the $d_{3z^2-r^2}$ orbital in the 326-LNO and 327-LNO compounds, we will use a bilayer two-orbital model in the following section.

Furthermore, we also calculated the band structure of the FM state for 326-LNO at 25 GPa. As shown in Figs. 3(b) and 3(c), the fully occupied $d_{3z^2-r^2}$ states have Mott-localized characteristics in both the bonding and antibonding states in 326-LNO far from the Fermi level. However, the spin-up and spin-down states are well-separated for the Ni's $d_{x^2-y^2}$ but with a fractional occupation of the spin-up bands, leading to metallic behavior.

Based on the discussion above, there are many similarities between 326-LNO and the previously well-discussed infinite-layer nickelate superconductors. The in-plane interorbital hopping between $d_{x^2-y^2}$ and $d_{3z^2-r^2}$ orbitals is nearly zero in those two systems [69] due to the lack of an apical oxygen [3]. Furthermore, the interlayer couplings are both
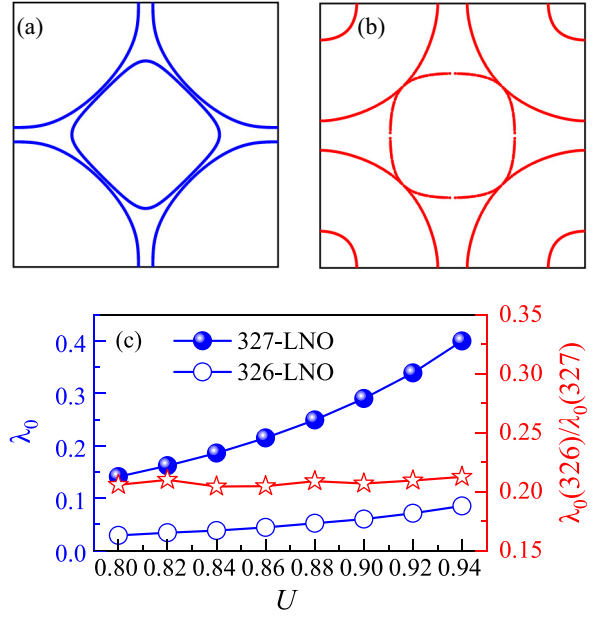
FIG. 4. (a), (b) FSs obtained from tight-binding calculations. (a) The hopping and crystal field were obtained from 326-LNO at 25 GPa. Here, the four-band e_g orbital model was considered with the overall filling $n = 5$ (2.5 electrons per site) in a bilayer lattice. Furthermore, we considered three neighbors of hopping in the xy plane and two neighbors of hopping between layers in our model calculation, while other long-range hoppings are ignored [62]. (b) The hopping and crystal field were obtained for 327-LNO at 25 GPa [9]. (c) The RPA calculated pairing strength λ_0 of the leading g-wave pairing state found for 326-LNO and the $s_\pm$-wave state for 327-LNO as a function of U (in units of eV) obtained from the bilayer model. Here we have set $U' = U/2$ and $J = J' = U/4$. The ratio λ_0(326-LNO)/λ_0(327-LNO) is also presented in red.

weak in those two systems, leading to an effective single-layer system. Furthermore, the $d_{x^2-y^2}$ orbital is the key orbital in both the two systems. Thus, in 326-LNO it is possible to obtain the same $d_{x^2-y^2}$-wave pairing symmetry obtained in infinite-layers nickelates [74,75], with only some additional modifications such as electron doping. This observation can provide an alternative way to explore the $d_{x^2-y^2}$-wave superconductivity nature in the infinite-layer nickelates or related systems, deserving more theoretical and experimental works.

C. RPA results for 326-LNO

As discussed in the previous section, based on calculations of magnetism, both the $s_\pm$-wave and d-wave pairing appear to be unlikely in 326-LNO. To better understand the superconducting pairing in 326-LNO, we performed multiorbital RPA calculations for the four-band e_g bilayer tight-binding model in Eq. (1).

As shown in Fig. 4(a), the FS obtained from the tight-binding model fits the DFT FS well, consisting of two sheets (α and β) made up primarily of the $d_{x^2-y^2}$ orbital. As a comparison, the model FS of 327-LNO is also shown in Fig. 4(b), where the hoppings, overall filling, and crystal-field splitting were taken from our previous study [9].
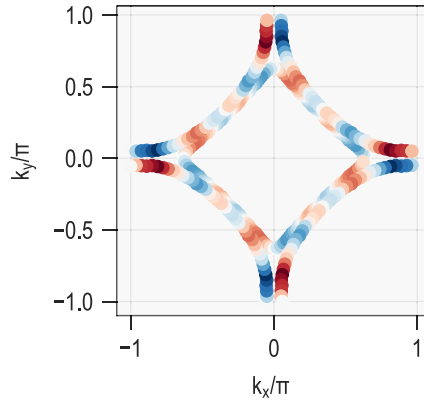
FIG. 5. The calculated RPA superconducting gap structure $g_\alpha(\mathbf{k})$ for momenta $\mathbf{k}$ on the FS of 326-LNO with g-wave symmetry. The sign of the gap is indicated by the colors (red = positive, blue = negative), and the gap magnitude by the color brightness.

FIG. 6. Projected band structures and density of states for the nonmagnetic state without interaction of 12126-HBCCO at (a) 0 GPa, and (b) 25 GPa, respectively. The Fermi level (zero energy) is marked by the horizontal dashed line. The coordinates of the high-symmetry points of the Brillouin zone of $P4/mmm$ 12126-HBCCO are $\Gamma = (0, 0, 0)$, $X = (0.5, 0, 0)$, $M = (0.5, 0.5, 0.5)$, $Z = (0, 0, 0.5)$, $R = (0, 0.5, 0.5)$, and $A = (0.5, 0.5, 0.5)$.

Figure 4(c) shows the RPA results for the pairing strength λ_0 of the leading pairing instability calculated from Eq. (3) for 326-LNO and 327-LNO as a function of the intra-orbital Coulomb repulsion U. Here we have set the inter-orbital Coulomb repulsion $U' = U/2$ and the Hund's rule coupling and pair hopping $J = J' = U/4$. For 327-LNO, the leading pairing state has $s_\pm$ symmetry, as we discussed before in Ref. [9], for all values of U. For 326-LNO, both $s_\pm$ and $d_{x^2-y^2}$-wave states are not competitive, and we instead find a leading g-wave state (see Fig. 5) for all values of U. As expected, in both cases, λ_0 increases with increasing U. More importantly, however, the leading g-wave state for 326-LNO has a significantly lower λ_0 (by about a factor of 5) compared to that of the leading $s_\pm$ state for 327-LNO. This provides evidence for a substantial qualitative difference between the two systems and shows that the 326-LNO system is far from a superconducting instability.

In addition, the calculated RPA gap function of 326-LNO shows a g-wave structure that is in phase between the two FS sheets, as shown in Fig. 5. This gap structure has higher harmonic contributions, leading to the additional nodes. The highly anisotropic structure and the large number of nodes are probably because of the competition of many interactions at different wave vectors q, including the local Coulomb repulsion. Increasing U further, the value of the coupling λ in the g channel does not increase substantially and remains small up to the critical $U = 1.01$ where the RPA finds a magnetic instability. This indicates that a possible superconducting instability is likely preempted by a magnetic instability in this system. Thus, our RPA results suggest that the 326-LNO system should not have a superconducting state, while 327-LNO should be superconducting, both predictions in good agreement with experiments [1,48]. This establishes substantial qualitative differences between the two systems.

As discussed before, one can understand the absence of an $s_\pm$ instability in 326-LNO from the fact that, compared to 327-LNO, the $d_{3z^2-r^2}$ orbital is much farther from the Fermi level, and therefore does not contribute to the low-energy physics, resulting in a much weaker interlayer coupling. In addition, the $d_{x^2-y^2}$ orbital is at quarter filling in 326-LNO. This electronic density is far from the typical density region

for which a single-band system like the cuprates displays d-wave superconductivity.

D. Electronic structure of reduced bilayer 12126-HBCCO

All the above discussions of 326-LNO suggest that the reduced 326 RP-BL system is very different from the 327 RP-BL system. The main reason for this difference is that the $d_{3z^2-r^2}$ orbital plays a different role in these two bilayer systems due to different crystal-field splittings Δ of the e_g orbitals with or without apical oxygen atoms. Next, let us briefly reexamine the typical reduced bilayer cuprate 12126-HBCCO to better understand the similarities and differences between the bilayer nickelates and cuprates.

12126-HBCCO forms a $P4/mmm$ tetragonal crystal structure with space group No. 123 [43], as shown in Fig. 1(c). Without pressure, near the Fermi level, the Bloch states are mainly composed of the Cu $3d$ orbitals that have much stronger hybridization with the O $2p$ orbitals than in 326-LNO and 327-LNO, as displayed in Fig. 6(a). Furthermore, this also suggests a smaller charge-transfer gap between the Cu d and O p-states than that in 327-LNO and 326-LNO, establishing the most fundamental universal difference between nickelates and cuprates. In addition, for 12126-HBCCO, the Fermi states have contributions from the Cu $d_{x^2-y^2}$ orbital. For both RP-BL and reduced RP-BL systems, the $d_{3z^2-r^2}$ orbital has a large hopping between the two Ni layers, while the $d_{x^2-y^2}$ has zero hopping because it lies in the xy plane. Hence, the Cu $d_{3z^2-r^2}$ orbital also displays a bonding-antibonding molecular-orbital splitting behavior with fully occupied character due to a large crystal-field splitting Δ of e_g orbitals, similar to 326-LNO, resulting in significant differences between RP-BL and reduced RP-BL systems. In this case, the bonding-antibonding state arises from the overlap between the $d_{3z^2-r^2}$

orbitals due to the bilayer geometry, where the apical O p_z is a bridge connecting two Ni sites in the 327-LNO that can enhance the bonding-antibonding splitting.

As displayed in Fig. 6(b), with increasing pressure, the bandwidth of the $d_{x^2-y^2}$ orbital of 12126-HBCCO substantially increases as compared to that at 0 GPa, implying an enhancement of the itinerant properties of the $3d$ electrons. Furthermore, the band structure of 12126-HBCCO also clearly indicates a self-hole-doping effect of the $d_{x^2-y^2}$ orbitals under pressure. According to the Bader charge analysis [76–78], the charge of Cu significantly decreases by about 0.13 electrons from 0 GPa to 25 GPa. This pressure-induced change of the electronic density is reminiscent of the previously studied two-leg iron ladder superconductors $BaFe_2X_3$ (X = S or Se) [79,80], where the self-doping effect under pressure induces superconductivity, as discussed previously using a two-orbital Hubbard model [81,82]. However, in our paper we do not find any obvious significant charge transfer for 326-LNO under pressure, establishing another important difference between the nickelates and the cuprates.

IV. CONCLUSIONS

In summary, here we have systematically studied the similarities and differences of the two bilayer nickelates 326-LNO and 327-LNO. We presented our rationale for the absence of superconductivity in 326-LNO under pressure by using DFT and RPA calculations. For both bilayer nickelates, the states near the Fermi level mainly arise from the Ni $3d$ orbitals, while most of the O $2p$ states are localized away from the Fermi energy. In addition, pressure increases the bandwidth of the Ni $3d$ states, leading to an enhanced itinerant behavior, which produces a reduced effective electronic correlation. In both 326-LNO and 327-LNO, the $d_{3z^2-r^2}$ orbital shows bonding-antibonding splitting states. The absence of the apical oxygen leads to a large crystal-field splitting between the e_g orbitals in 326-LNO, resulting in the $d_{3z^2-r^2}$ orbital being far away from the Fermi level and thus reducing its importance. This also results in a smaller bandwidth for the $d_{x^2-y^2}$ orbital and a reduced bonding-antibonding energy splitting of the $d_{3z^2-r^2}$ orbital, as compared to 327-LNO. Moreover, the in-plane hybridization between $d_{x^2-y^2}$ and $d_{3z^2-r^2}$ is found to be very small in 326-LNO, much smaller than in 327-LNO.

In addition, using RPA calculations, we have found that superconducting pairing correlations are significantly weaker in 326-LNO relative to 327-LNO. Due to a much reduced interlayer coupling, the leading $s_\pm$-wave state found for 327-LNO is suppressed for 326-LNO. Moreover, we have found that a low-spin FM state has the lowest energy among the five magnetic configurations studied, much lower than the C-AFM state, indicating a large in-plane FM coupling in 326-LNO. This, and the fact that the in-plane $d_{x^2-y^2}$ orbitals are quarter-filled, explains why AFM fluctuation driven d-wave pairing correlations are similarly suppressed in 326-LNO.

Similar to 326-LNO, the $d_{3z^2-r^2}$ orbital also displays a bonding-antibonding state splitting character in the cuprate 12126-HBCCO, suggesting a common electronic structure in the bilayer lattice. However, as a fundamental difference between cuprates and nickelates, the Cu $3d$ orbitals in the cuprates are highly hybridized with the O $2p$ orbitals, leading
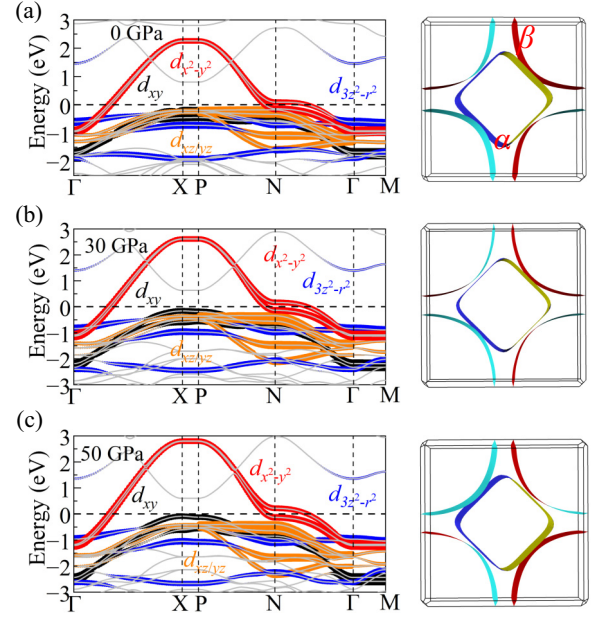
FIG. 7. Projected band structures and FSs of the nonmagnetic phase of the $I4/mmm$ 326-LNO structures without any interaction at (a) 0 GPa, (b) 30 GPa, and (c) 50 GPa, respectively. The weight of each Ni orbital is given by the size of the circles. The Fermi level (zero energy) is marked by the horizontal dashed line. The coordinates of the high-symmetry points of the Brillouin zone are $\Gamma = (0, 0, 0)$, $X = (0, 0, 0.5)$, $P = (0.25, 0.25, 0.25)$, $N = (0, 0.5, 0)$, and $M = (0.5, 0.5, -0.5)$.

to a much smaller charge-transfer gap. Moreover, we found a strong pressure induced self-doping effect of the $d_{x^2-y^2}$ orbital in 12126-HBCCO, where the charge of the Cu states is significantly reduced by about 0.13 electrons when changing pressure from 0 GPa to 25 GPa. However, we do not observe such a change of the electronic density in 326-LNO under pressure, indicating another important difference between the nickelate and the cuprate bilayer systems.

ACKNOWLEDGMENTS

TABLE II. Energy differences (meV/Ni) and calculated magnetic moment (μ_B/Ni) for the various input spin configurations used here for the LDA + U + J formalism ($U = 3.8$ eV and $J = 0.61$ eV). The FM configuration is taken as the energy of reference.

Magnetism	Energy	Magnetic moment
A-AFM	0.15	0.498
FM	0	0.498
G-AFM	47.09	0.001
C-AFM	46.11	0.100
stripe-AFM	21.70	0.374

TABLE III. Energy differences (meV/Ni) and calculated magnetic moment (μ_B/Ni) for the various input spin configurations used here of LSDA $+ U$ ($U_{\text{eff}} = 4$ eV). The FM configuration is taken as the energy of reference.

Magnetism	Energy	Magnetic moment
A-AFM	0.48	0.597
FM	0	0.585
G-AFM	185.54	0.416
C-AFM	181.29	0.421
stripe-AFM	66.17	0.549

APPENDIX

1. Electronic structures and Fermi surface for different pressures

As shown in Fig. 7, the electronic structures of 326-LNO are very similar under pressure. The $d_{x^2-y^2}$ orbital contributes the most to the Fermi level, while other d orbitals are fully occupied. The FS are contributed by two sheets (α and β) made almost entirely of the single $d_{x^2-y^2}$ orbital. The pressure increases the bandwidth of Ni's $3d$ states, leading to an enhanced itinerant behavior, thus also leading to reduced effective electronic correlations U/W.

2. Additional discussion about magnetism in 326-LNO at 25 GPa

In addition, we calculated the magnetic correlations in the LDA $+ U$ format with double-counting item [56] by using the calculated U and J for 327-LNO ($U = 3.8$ eV and $J = 0.61$ eV) [17]. As shown in Table II, the FM state still has the lowest energy among all the candidates. Alternatively, we also considered the local spin density approach (LSDA) plus U by using the Dudarev's rotationally invariant formulation [83] (LSDA $+ U_{\text{eff}} = 4$ eV [69]), where some correlations have already been introduced to the LSDA portion. The conclusion is not changed, namely, the FM state has the lowest energy (see Table III), in agreement with our analysis in the main text. Based on all these results, the conclusion of having FM spin correlations in the 326-LNO is robust, although quantum fluctuations need to be better incorporated to fully confirm our results.
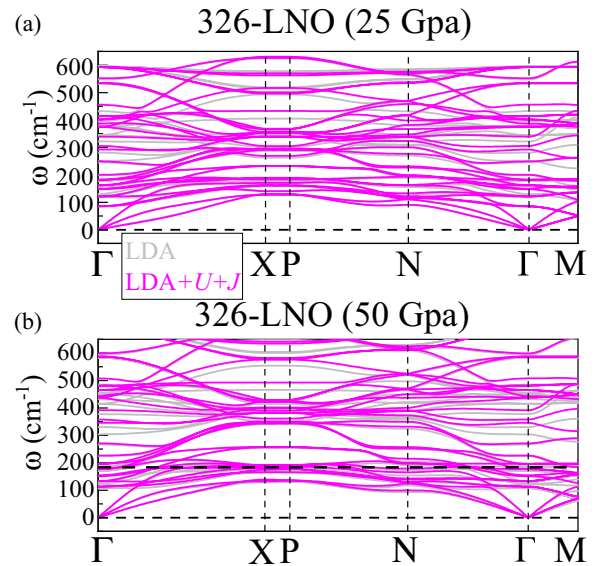
FIG. 8. Phonon spectrum of the $I4/mmm$ phase of 326-LNO at (a) 25 GPa and (b) 50 GPa, respectively. Here, we calculated the phonon spectra for the cases of LDA and LDA plus U and J ($U = 4.75$ eV and $J = 0.68$ eV) with the Liechtenstein formulation within the double-counting item [56], respectively, as distinguished by gray and pink. The coordinates of the high-symmetry points of the Brillouin zone are $\Gamma = (0, 0, 0)$, $X = (0, 0, 0.5)$, $P = (0.25, 0.25, 0.25)$, $N = (0, 0.5, 0)$, and $M = (0.5, 0.5, -0.5)$.

3. Phonon spectrum of 326-LNO at 25 and 50 GPa

The recent experiments do not observe a structural phase transition under pressure, at least in the pressure region they studied (up to 25.3 GPa) [48]. To better under the structural stability of the 326-LNO compound, we calculated the phonon spectra for 25 and 30 GPa, respectively. Here, a $2 \times 2 \times 1$ conventional cell structure of the $I4/mmm$ phase was used in the phonon calculation by using the density functional perturbation theory approach [84,85], analyzed by the PHONONPY software in the primitive unit cell [86,87]. As displayed in Fig. 8, the $I4/mmm$ structure of 326-LNO is stable at 25 GPa and 50 GPa, in agreement with the experimental results [48].

[1] H. Sun, M. Huo, X. Hu, J. Li, Y. Han, L. Tang, Z. Mao, P. Yang, B. Wang, J. Cheng, D.-X. Yao, G.-M. Zhang, and M. Wang, Nature (London) **621**, 493 (2023).

[2] Z. Luo, X. Hu, M. Wang, W. Wu, and D.-X. Yao, Phys. Rev. Lett. **131**, 126001 (2023).

[3] Y. Zhang, L.-F. Lin, A. Moreo, and E. Dagotto, Phys. Rev. B **108**, L180510 (2023).

[4] Q.-G. Yang, D. Wang, and Q.-H. Wang, Phys. Rev. B **108**, L140505 (2023).

[5] H. Sakakibara, N. Kitamine, M. Ochi, and K. Kuroki, arXiv:2306.06039.

[6] Y. Gu, C. Le, Z. Yang, X. Wu, and J. Hu, arXiv:2306.07275.

[7] Y. Shen, M. Qin, and G.-M. Zhang, Chinese Phys. Lett. **40**, 127401 (2023).

[8] Y.-B. Liu, J.-W. Mei, F. Ye, W.-Q. Chen, and F. Yang, Phys. Rev. Lett. **131**, 236002 (2023).

[9] Y. Zhang, L.-F. Lin, A. Moreo, T. A. Maier, and E. Dagotto, arXiv:2307.15276v3.

[10] Y.-F. Yang, G.-M. Zhang, and F.-C. Zhang, Phys. Rev. B **108**, L201108 (2023).

[11] C. Lu, Z. Pan, F. Yang, and C. Wu, arXiv:2307.14965.

[12] H. Oh and Y. H. Zhang, Phys. Rev. B **108**, 174511 (2023).

[13] Z. Liao, L. Chen, G. Duan, Y. Wang, C. Liu, R. Yu, and Q. Si, Phys. Rev. B **108**, 214522 (2023).

[14] X.-Z. Qu, D.-W. Qu, J. Chen, C. Wu, F. Yang, W. Li, and G. Su, Phys. Rev. Lett. **132**, 036502 (2024).

[15] Y. Cao and Y.-F. Yang, arXiv:2307.06806.

[16] F. Lechermann, J. Gondolf, S. Bötzel, and I. M. Eremin, Phys. Rev. B **108**, L201121 (2023).

[17] V. Christiansson, F. Petocchi, and P. Werner, Phys. Rev. Lett. **131**, 206501 (2023).

[18] Z. Liu, M. Huo, J. Li, Q. Li, Y. Liu, Y. Dai, X. Zhou, J. Hao, Y. Lu, M. Wang, and W.-H. Wen, arXiv:2307.02950.

[19] W. Wu, Z. Luo, D.-X. Yao, and M. Wang, arXiv:2307.05662.

[20] D. A. Shilenko and I. V. Leonov, Phys. Rev. B **108**, 125105 (2023).

[21] X. Chen, P. Jiang, J. Li, Z. Zhong, and Y. Lu, arXiv:2307.07154.

[22] Y. Zhang, D. Su, Y. Huang, H. Sun, M. Huo, Z. Shan, K. Ye, Z. Yang, R. Li, M. Smidman, M. Wang, L. Jiao, and H. Yuan, arXiv:2307.14819.

[23] J. Hou, P. T. Yang, Z. Y. Liu, J. Y. Li, P. F. Shan, L. Ma, G. Wang, N. N. Wang, H. Z. Guo, J. P. Sun, Y. Uwatoko, M. Wang, G.-M. Zhang, B. S. Wang, and J.-G. Cheng, Chin. Phys. Lett. **40**, 117302 (2023).

[24] K. Jiang, Z. Wang, and F. Zhang, Chin. Phys. Lett. **41**, 017402 (2024).

[25] J. Huang, Z. D. Wang, and T. Zhou, Phys. Rev. B **108**, 174501 (2023).

[26] Y. Zhang, L.-F. Lin, A. Moreo, T. A. Maier, and E. Dagotto, Phys. Rev. B **108**, 165141 (2023).

[27] Q. Qin and Y.-F. Yang, Phys. Rev. B **108**, L140504 (2023).

[28] Y.-H. Tian, Y. Chen, J.-M. Wang, R.-Q. He, and Z.-Y. Lu, arXiv:2308.09698.

[29] Y.-C. Lu, M. Li, Z.-Y. Zeng, W. Hou, J. Wang, F. Yang, and Y.-Z. You, arXiv:2308.11195.

[30] R. Jiang, J. Hou, Z. Fan, Z.-J. Lang, and W. Ku, arXiv:2308.11614.

[31] Z. Luo, B. Lv, M. Wang, W. Wu, and D.-X. Yao, arXiv:2308.16564.

[32] J. Yang, H. Sun, X. Hu, Y. Xie, T. Miao, H. Luo, H. Chen, B. Liang, W. Zhu, G. Qu, C.-Q. Chen, M. Huo, Y. Huang, S. Zhang, F. Zhang, F. Yang, Z. Wang, Q. Peng, H. Mao, G. Liu, Z. Xu, T. Qian, D.-X. Yao, M. Wang, L. Zhao, and X. J. Zhou, arXiv:2309.01148.

[33] M. Zhang, C. Pei, Q. Wang, Y. Zhao, C. Li, W. Cao, S. Zhu, J. Wu, and Y. Qi, J. Mater. Sci. Technol. **185**, 147 (2024).

[34] J.-X. Zhang, H.-K. Zhang, Y.-Z. You, and Z.-Y. Weng, arXiv:2309.05726.

[35] Z. Pan, C. Lu, F. Yang, and C. Wu, arXiv:2309.06173.

[36] B. Geisler, J. J. Hamlin, G. R. Stewart, R. G. Hennig, and P. J. Hirschfeld, arXiv:2309.15078.

[37] H. Yang, H. Oh, and Y.-H. Zhang, arXiv:2309.15095.

[38] L. C. Rhodes and P. Wahl, arXiv:2309.15745.

[39] H. LaBollita, V. Pardo, M. R. Norman, and A. S. Botana, arXiv:2309.17279.

[40] G. Wang, N. N. Wang, J. Hou, L. Ma, L. F. Shi, Z. A. Ren, Y. D. Gu, X. L. Shen, H. M. Ma, P. T. Yang, Z. Y. Liu, H. Z. Guo, J. P. Sun, G. M. Zhang, J. Q. Yan, B. S. Wang, Y. Uwatoko, and J.-G. Cheng, arXiv:2309.17378.

[41] T. Kaneko, H. Sakakibara, M. Ochi, and K. Kuroki, arXiv:2310.01952.

[42] C. Lu, Z. Pan, F. Yang, and C. Wu, arXiv:2310.0291.

[43] S. M. Loureiro, E. V. Antipov, J. L. Tholence, J. J. Capponi, O. Chmaissem, Q. Huang, and M. Marezio, Physica (Amsterdam) **217**, 253 (1993).

[44] V. V. Poltavets, M. Greenblatt, G. H. Fecher, and C. Felser, Phys. Rev. Lett. **102**, 046405 (2009).

[45] N. apRoberts-Warren, J. Crocker, A. P. Dioguardi, K. R. Shirer, V. V. Poltavets, M. Greenblatt, P. Klavins, and N. J. Curro, Phys. Rev. B **88**, 075124 (2013).

[46] S. Sarkar, I. Dasgupta, M. Greenblatt, and T. Saha-Dasgupta, Phys. Rev. B **84**, 180411(R) (2011).

[47] A. S. Botana, V. Pardo, W. E. Pickett, and M. R. Norman, Phys. Rev. B **94**, 081105(R) (2016).

[48] Z. Liu, H. Sun, M. Huo, X. Ma, Y. Ji, E. Yi, L. Li, H. Liu, J. Yu, Z. Zhang, Z. Chen, F. Liang, H. Dong, H. Guo, D. Zhong, B. Shen, S. Li, and M. Wang, Sci. China Phys. Mech. Astron. **66**, 217411 (2023).

[49] G. Kresse and J. Hafner, Phys. Rev. B **47**, 558 (1993).

[50] G. Kresse and J. Furthmüller, Phys. Rev. B **54**, 11169 (1996).

[51] P. E. Blöchl, Phys. Rev. B **50**, 17953 (1994).

[52] J. P. Perdew, K. Burke, and M. Ernzerhof, Phys. Rev. Lett. **77**, 3865 (1996).

[53] A. A. Mostofi, J. R. Yates, Y. S. Lee, I. Souza, D. Vanderbilt, and N. Marzari, Comput. Phys. Commun. **178**, 685 (2008).

[54] A. Kokalj, J. Mol. Graphics Modell. **17**, 176 (1999).

[55] K. Momma and F. Izumi, J. Appl. Crystallogr. **44**, 1272 (2011).

[56] A. I. Liechtenstein, V. I. Anisimov, and J. Zaanen, Phys. Rev. B **52**, R5467(R) (1995).

[57] V. Pardo and W. E. Pickett, Phys. Rev. B **83**, 245128 (2011).

[58] T. A. Maier and D. J. Scalapino, Phys. Rev. B **84**, 180513(R) (2011).

[59] V. Mishra, T. A. Maier, and D. J. Scalapino, Sci. Rep. **6**, 32078 (2016).

[60] T. A. Maier, V. Mishra, G. Balduzzi, and D. J. Scalapino, Phys. Rev. B **99**, 140504(R) (2019).

[61] P. M. Dee, S. Johnston, and T. A. Maier, Phys. Rev. B **105**, 214502 (2022).

[62] See Supplemental Material at http://link.aps.org/supplemental/10.1103/PhysRevB.109.045151 for the detailed hoppings and crystal field splittings used in our RPA study for 326-LNO.

[63] K. Kubo, Phys. Rev. B **75**, 224509 (2007).

[64] S. Graser, T. A. Maier, P. J. Hirschfeld, and D. J. Scalapino, New J. Phys. **11**, 025016 (2009).

[65] M. Altmeyer, D. Guterding, P. J. Hirschfeld, T. A. Maier, and R. Valentí, and D. J. Scalapino, Phys. Rev. B **94**, 214515 (2016).

[66] A. T. Rømer, T. A. Maier, A. Kreisel, I. Eremin, and P. J. Hirschfeld, and B. M. Andersen, Phys. Rev. Res. **2**, 013108 (2020).

[67] S. Bhattacharyya, P. J. Hirschfeld, T. A. Maier, and D. J. Scalapino, Phys. Rev. B **101**, 174509 (2020).

[68] Here, the primitive unit cells with two Ni atoms were considered to calculate band structures and FSs. For 326-LNO, the lattice constants and atomic positions were fully relaxed within the PAW method with the PBE exchange potential. For the 327 type, we used the optimized structure obtained from our previous work [9].

[69] Y. Zhang, L.-F. Lin, W. Hu, A. Moreo, S. Dong, and E. Dagotto, Phys. Rev. B **102**, 195117 (2020).

[70] In addition, we also studied magnetic correlations for 326-LNO using other two different sets of parameters (see Appendix for more details). Our conclusions are not changed, namely, the FM state has the lowest energy among all the candidates, in agreement with our discussion in the main text. Note that the local electronic correlation effects are treated at a static mean-field level in the DFT $+ U$ calculations. This system may not develop long-range FM order by considering the quantum

fluctuations, because quantum fluctuations are ignored in the DFT $+\,U$ calculations.

[71] D. Vollhardt, N. Blumer, K. Held, and M. Kollar, *Lecture Notes in Physics*, Vol 580, Springer, Berlin, Heidelberg 2020; P. Werner, X. Chen, and E. Gull, Phys. Rev. Res. **2**, 023037 (2020).

[72] L. F. Lin, Y. Zhang, G. Alvarez, A. Moreo, and E. Dagotto, Phys. Rev. Lett. **127**, 077204 (2021).

[73] L. F. Lin, Y. Zhang, G. Alvarez, M. A. McGuire, A. F. May, A. Moreo, and E. Dagotto, Commun. Phys. **6**, 199 (2023).

[74] X. Wu, D. DiSante, T. Schwemmer, W. Hanke, H. Y. Hwang, S. Raghu, and R. Thomale, Phys. Rev. B **101**, 060504(R) (2020).

[75] H. Sakakibara, H. Usui, K. Suzuki, T. Kotani, H. Aoki, and K. Kuroki, Phys. Rev. Lett. **125**, 077003 (2020).

[76] R. F. W. Bader, *Encyclopedia of Computational Chemistry* (Wiley, Chichester, UK, 2002).

[77] W. Tang, E. Sanville, and G. Henkelman, J. Phys.: Condens. Matter **21**, 084204 (2009).

[78] G. Henkelman, A. Arnaldsson, and H. Jónsson, Comput. Mater. Sci. **36**, 354 (2006).

[79] Y. Zhang, L. F. Lin, J. J. Zhang, E. Dagotto, and S. Dong, Phys. Rev. B **95**, 115154 (2017).

[80] Y. Zhang, L. F. Lin, J. J. Zhang, E. Dagotto, and S. Dong, Phys. Rev. B **97**, 045119 (2018).

[81] N. D. Patel, A. Nocera, G. Alvarez, R. Arita, A. Moreo, and E. Dagotto, Phys. Rev. B **94**, 075119 (2016).

[82] N. D. Patel, A. Nocera, G. Alvarez, A. Moreo, and E. Dagotto, Phys. Rev. B **96**, 024520 (2017).

[83] S. L. Dudarev, G. A. Botton, S. Y. Savrasov, C. J. Humphreys, and A. P. Sutton, Phys. Rev. B **57**, 1505 (1998).

[84] S. Baroni, P. Giannozzi, and A. Testa, Phys. Rev. Lett. **58**, 1861 (1987).

[85] X. Gonze, Phys. Rev. A **52**, 1086 (1995); X. Gonze, X. Gonze, *ibid.* **52**, 1096 (1995).

[86] L. Chaput, A. Togo, I. Tanaka, and G. Hug, Phys. Rev. B **84**, 094302 (2011).

[87] A. Togo and I. Tanaka, Scr. Mater. **108**, 1 (2015).